

# Micromachined 2-D scanner for 3-D optical coherence tomography

J.T.W. Yeow<sup>a,c,\*</sup>, V.X.D. Yang<sup>b,d</sup>, A. Chahwan<sup>a</sup>, M.L. Gordon<sup>b,d</sup>, B. Qi<sup>b</sup>,  
I.A. Vitkin<sup>b,d</sup>, B.C. Wilson<sup>b,d</sup>, A.A. Goldenberg<sup>a</sup>

<sup>a</sup> Robotics and Automation Laboratory, Department of Mechanical and Industrial Engineering, University of Toronto, Canada

<sup>b</sup> Ontario Cancer Institute, Princess Margaret Hospital, University Health Network, Canada

<sup>c</sup> Department of Systems Design Engineering, University of Waterloo, Canada

<sup>d</sup> Department of Medical Biophysics, University of Toronto, Canada

Received 24 February 2004; received in revised form 22 June 2004; accepted 23 June 2004

Available online 29 July 2004

## Abstract

With the inherent advantages of micromachining technologies such as small size, small mass, low cost, low power consumption and high reliability, there will be radical changes to biomedical devices and how clinical diagnoses are made. One of the most promising applications of microtechnologies is in the field of medical science. This paper presents a potentially low voltage high electrostatic torque micromachined mirror capable of two-dimensional (2-D) scans (simultaneous transverse and longitudinal scans) for optical coherence tomographic imaging. When the micro-mirror is integrated with an optical coherence tomography (OCT) system, three-dimensional (3-D) sample images can be obtained in one longitudinal scan period. 3-D images of internal-organs of fruit fly (*Drosophila melanogaster*) and its larva are acquired using the micromachined-based OCT system. The dimension of the micromachined mirror is 1000  $\mu\text{m} \times 1000 \mu\text{m}$ . The entire MEMS scanner is made of single-silicon crystal, to act as mechanical reinforcement counteracting the inherent stresses of the deposited thin films on the mirror. The scanning mirror is actuated electrostatically.

© 2004 Elsevier B.V. All rights reserved.

**Keywords:** MEMS; Micromachined; Optical scanner; Optical coherence tomography; Endoscope

## 1. Introduction

The emergence of minimally invasive diagnostics and therapeutics in modern high-tech medicine has generated an unmet demand in miniaturized tomographic devices, forecasting an interesting future in biomedical imaging [1]. In the past decade, there have been major advances in optics-based techniques, exploiting the unique features of light-tissue interactions [2]. The micromachining technology highly complements established optical medical imaging modalities. Applications such as miniature handheld tomographic devices, endoscopic tomographic devices, and catheter-based

tomographic devices are just some examples where potential clinical benefit can be realized using micromachining technology [3,4]. The ability to fabricate micromachined mirrors and other optical elements on the order of hundreds of micrometers in dimensions has stimulated research into new applications. Low-inertia scanners that deflect light using a micro mirror of small mass have desirable features such as small wobble and jitter, high scanning speed and accuracy, and are capable of precision positioning. As a result, miniaturized low-inertia micro mirrors are often the obvious choice for high-performance and cost-effective optical scanners.

In the past decade, micromachining technology is making a big impact in many fields, especially for biomedical instruments. The small size, and low mass of micromachines make medical instruments incorporating the technology portable. Micromachines are constructed using similar batch fabrication techniques as integrated circuit (IC) fabrication. Many

\* Corresponding author. Present address: 200 University Avenue West, Waterloo, Ont., Canada N2L 3G1 Tel.: +1 519 888 4567x2152; fax: +1 519 746 4791.

E-mail address: [jyeow@engmail.uwaterloo.ca](mailto:jyeow@engmail.uwaterloo.ca) (J.T.W. Yeow).

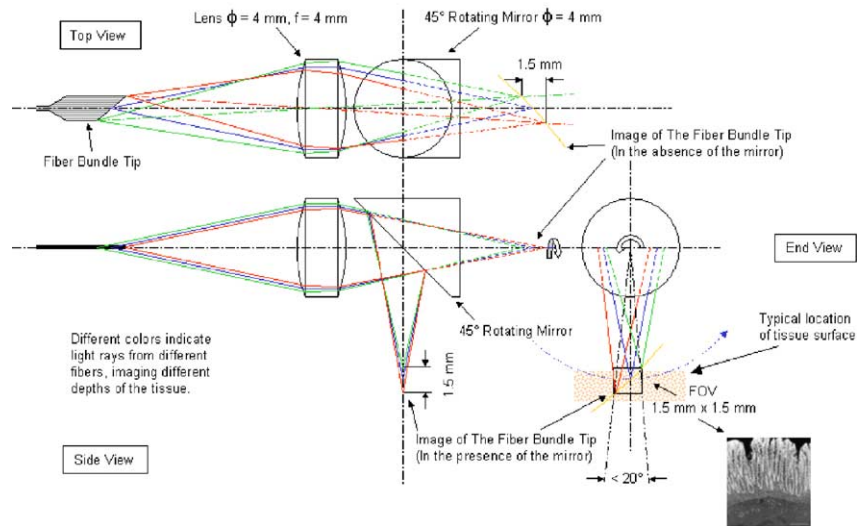


Fig. 1. The current tip design of the endoscopic coherence optical microscope using conventional techniques (*note*: not to scale).

micromachined devices can be fabricated on the same silicon wafer at the same time, thereby reducing the cost of each device. The cost effectiveness of each device makes it disposable; therefore, increasing the usability and serviceability of medical instruments. One of the medical instruments that can benefit from the significant improvement in equipment performance and quality of patient diagnosis made by incorporating micromachining technology is the Endoscopic Coherence Optical Microscope (ECOM). Optical coherence tomography (OCT) is an emerging technology for performing high-resolution cross-sectional imaging. OCT is analogous to ultrasound imaging, except that it uses light instead of sound. OCT can provide cross-sectional images of tissue structure on the micron scale *in situ* and in real time [5].

Presently, ECOM is being developed as a joint project between the Ontario Cancer Institute (OCI), and St. Michael's Hospital (SMH). It utilizes a novel multiple fiber design [6] incorporating video-rate optical coherence tomography technology [7]. One of the critical components is the performance of the scanning mirror located at the tip of the device. The current design of ECOM uses a conventional rotating mirror driven by a guide-wire going through the entire length of the endoscope to achieve scanning motion. The guide-wire, and hence the mirror, is rotated  $360^\circ$  using an external motor. This mechanism is not only cumbersome but also places serious limitations on the performance of the ECOM system. Three factors are involved: (i) since the OCT technology is an interferometric technique, any wave-front/polarization distortion of the light while it is traversing through the fibre can greatly change the signal amplitude. A rotating guide-wire extending the entire length of the endoscope is a source of unwanted vibrations and exerts changing mechanical stress to the fibres, thus degrading the image quality; (ii) imaging is only possible over a small sector angle ( $\sim 20^\circ$ ), resulting in a duty cycle less than 10% in terms of light source power utilization;

(iii) Doppler blood flow measurements [21,22] similar to the Doppler ultrasound can be realized in the ECOM system. The conventional scanning system using bulk optics is shown in Fig. 1. Doppler measurements have more stringent requirement on stabilizing the interferometer of the ECOM system, which includes the ECOM tip and the fibers traversing in the endoscope. Here, vibration introduces large random errors on the flow velocity measurements, limiting the frame rate in Doppler measurements. Given the problems experienced by the current scanning systems, a scanning device with integrated actuating mechanism and micro mirror is clearly needed so that the mirror scanning motion is less susceptible to external vibration while providing higher duty cycle ratio. The integrated device should also satisfy the following engineering parameters and quality: (i) small size; (ii) low power;

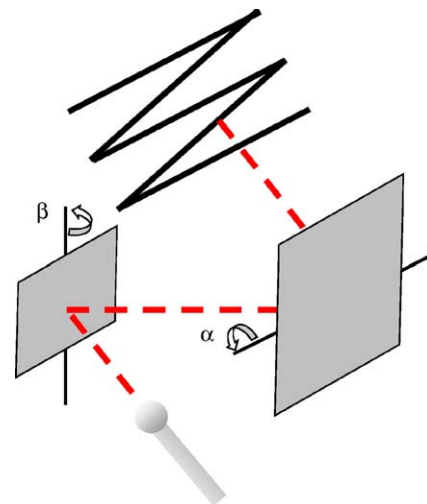


Fig. 2. Raster scanning achieved by using a combination of vertical and horizontal scanners.

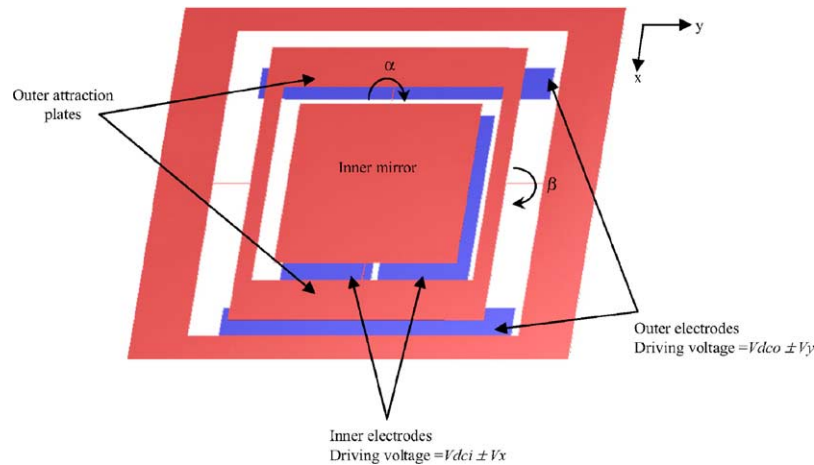


Fig. 3. Layout of 2D scanning micro-mirror.

(iii) low cost; and (iv) reliable. Micromachining technology with its inherent advantages is ideal for this purpose.

## 2. Previous work

Previous work involving micromachined scanners that have been implemented is reported in [8–13]. The previous efforts were focused on fabricating mirrors on the micron scale. Issues such as low driving voltages, large scan angles, large mirror surface of high optical quality, compact overall design, system performance of the scanner and actuating mechanism when integrated with the ECOM have not been addressed. Furthermore, there is an increasing need to achieve raster scans for imaging tissue planes rather than line scans. Most of the scanning mirrors demonstrated to date involved a combination of two 1-D scanning mirrors [8,11]. One mirror scans horizontally and the other mirror scans vertically, thus performing raster-scanning collectively. Fig. 2 shows that 2-D raster scanning can be achieved by a combination of two 1-D scanning mirrors. However, cascaded 1-D scanners have several disadvantages. A second mirror larger than the horizontal scan length of the first mirror is required to reflect the beam. This restriction results in low resonant frequency and also large overall size of the scanner, thereby failing to achieve the initial purpose of compact size and small mass. Micromachined mirrors with two axes of rotation have also been demonstrated in [14]. However, these two degree-of-freedom (DoF) scanners have high driving voltages, which are not suitable for in vivo biomedical applications such as endoscopic imaging.

The ideal scanning device would require low driving voltages for large angular scans. The scanning device should be capable of providing slow scan in one axis and fast scan in the orthogonal axis to achieve raster scanning and maintain good spatial scan resolution. In addition, the quality of the image resolution is proportional to the size of the reflective

surface of the scanning device. Therefore, the mirror of the scanner should be large so as to improve the image quality.

## 3. 2-D scanner architecture

The 2-D micromachined scanner is composed of two outer attraction plates and an inner scanning mirror. The schematic diagram of the 2-D micromachined scanner and the electrodes are shown in Fig. 3. The entire scanner structure is electrically grounded. The difference in voltage potential between the scanner and its electrodes generate the electrostatic fields. Two outer electrodes that are placed parallel to the y-axis attract the outer attraction plates for the  $\beta$ -scan. A second pair of electrodes is placed orthogonally to the y-axis and rotates the mirror plate about the x-axis for  $\alpha$ -scan. The combine rotation of the attraction plates and mirror about the x- and y-axes performs raster scanning. The mirror plate has a dimension of  $1000\text{ }\mu\text{m} \times 1000\text{ }\mu\text{m}$  and provides the slow axis scan. The entire scanner structure has a dimension of  $1400\text{ }\mu\text{m} \times 1700\text{ }\mu\text{m}$  and is the fast axis scan. The scan-

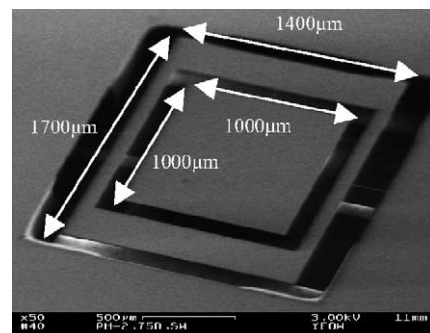


Fig. 4. Scanning electron microscope picture of micromachined scanner. The inner mirror has dimensions of  $1000\text{ }\mu\text{m} \times 1000\text{ }\mu\text{m}$ . The entire scanner structure ( $1400\text{ }\mu\text{m} \times 1700\text{ }\mu\text{m}$ ) is suspended by a pair of torsion bars with dimensions of  $200\text{ }\mu\text{m} \times 6\text{ }\mu\text{m} \times 1.1\text{ }\mu\text{m}$ .

ning electron microscope picture of the scanner is shown in Fig. 4.

#### 4. Mathematical model

The suspended mirror structures are actuated by electrostatic forces. Electrostatic actuation is chosen because it is well understood, and easy to implement [8,9,15].

The scanning capability is achieved by the simultaneous actuation of the mirror and the attraction plates. The electrostatic torques model of the mirror plate is complex because the rotating axis ( $\alpha$ -scan) of mirror moves with the outer attraction plates as the plates are rotated about their axis of rotation ( $\beta$ -scan). Therefore, the mirror is subject to varying electrostatic forces as it moves in two degree-of-freedom motion in space. Throughout the period of a raster scan, the electrostatic fields are not only changing in the direction along  $y$ -axis but also along the  $x$ -axis (in the case of the attraction plates). The electrostatic torques on the scanning mirror is expressed as [15]:

$$T_{\alpha}^i(V_i) = \frac{1}{2} \epsilon_0 V_i^2 \iint_S y \left( \frac{\sin \gamma}{\gamma} \frac{1}{d - y \cos \beta \sin \alpha + x \sin \beta} \right)^2 \times dS \quad (1)$$

where  $\gamma$  is the angle between the virtual extension of the outer attraction plates and the electrode plane.

The total electrostatic torques on the mirror is the sum of the torques generated from the two inner electrodes:

$$T_{\alpha}^T = \sum_{i=1}^2 T_{\alpha}^i(V_i) \quad (2)$$

The two inner electrodes are biased by a dc voltage  $V_{dci}$ , and modulated by small oscillating waveforms  $v_y$  ( $V_1 = V_{dci} + v_x$ ,  $V_2 = V_{dci} - v_x$ ). Previous study has shown that the dc-bias improves the linearity of the scanning sweep [16]. Furthermore, the electrostatic forces are a function of the square of the applied voltage, therefore it is desirable to have a dc-bias so that the resultant voltage is unipolar and the mirror is driven at the same frequency as the applied voltage rather than twice that frequency. The mechanical torques of

the restoring the torsion bars to the original shape is given by [17]:

$$T_m = 2 \frac{Gwt^3}{3l} \alpha \left[ 1 - \frac{192}{\pi^5} \frac{t}{w} \tanh \left( \frac{\pi w}{2t} \right) \right] \quad (3)$$

where  $w$  is the width of the mirror torsion bars,  $t$  the thickness of the torsion bars,  $G$  the shear modulus of the torsion bars,  $l$  the length of the torsion bars.

The width of the inner torsion bars is  $6 \mu\text{m}$ , the thickness is  $1.1 \mu\text{m}$ , and the length is  $100 \mu\text{m}$ .

$$T_{\alpha}^T = T_m \quad (4)$$

The solution of Eq. (4) represents the equilibrium of the mechanical torques experienced by the torsion bars and the electrostatic torques generated by the electrostatic fields on the mirror. The degree of  $\alpha$ -scan can be determined when given outer electrode bias voltages to rotate the scanner to  $\beta$ , inner electrode bias voltages, and the physical dimensions of mirror and torsion bars.

The electrostatic forces acting on the outer attraction plates rotate the entire scanner structure about the  $x$ -axis for the  $\alpha$ -scan.

The electrostatic 1-D model of the outer attraction plate is shown in Fig. 5. This model makes two assumptions [18]: (i) the intersection,  $A$ , of the virtual extension of the scanner structure and the electrodes acts a centre where the electrostatic field arcs arise; (ii) the electrostatic field strength is uniform along the axis parallel to the axis of rotation.  $L_c$  is the distance from the axis of rotation ( $O$ ) to the inner edge of the attraction plates.  $L_{\text{eff}}$  is the length of the electrodes. We assume that  $L_{\text{eff}}$  is also the effective length of the attraction plates that is subject to the electrostatic forces. The two electrodes are biased by a dc voltage  $V_{dco}$ , and modulated by small oscillating waveforms  $v_y$  ( $V_3 = V_{dco} + v_y$ ,  $V_4 = V_{dco} - v_y$ ).

The derivation of the electrostatic torque for 1-D scanner is well documented [11,18]. The electrostatic torques generated by the two electrodes are  $T_{e1}$  and  $T_{e2}$ , respectively. The total electrical torques on the attraction plates is:

$$\sum T_e = T_{e1} - T_{e2} \quad (5)$$

where

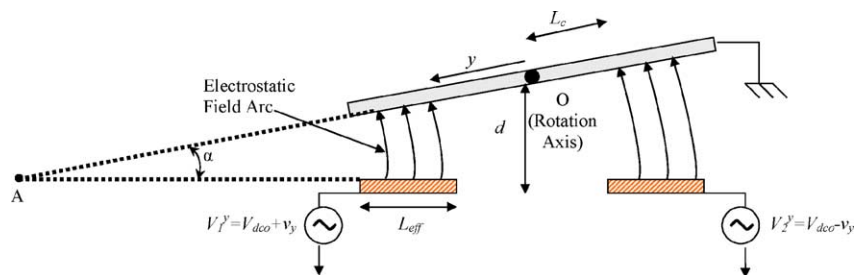


Fig. 5. Analytical model of the attraction plate.

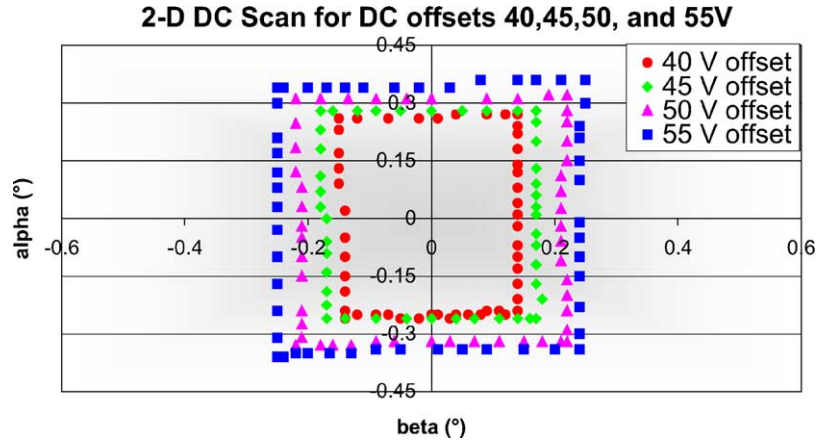


Fig. 6. Perimeter 2-D scans with different offset voltages.

$$\begin{aligned}
 T_{e1} &= \frac{\epsilon V_3^2 W}{2\beta^2} \int_{L_c}^{L_c+L_{eff}} \frac{y}{((d/\sin\beta) - y)^2} dy \\
 &= \frac{\epsilon V_3^2 W}{2\beta^2} \left[ \ln \left| \frac{d}{\sin\beta} - L_\beta \right| + \frac{d/\sin\beta}{(d/\sin\beta) - L_\beta} \right. \\
 &\quad \left. - \ln \left| \frac{d}{\sin\beta} - L_c \right| - \frac{d/\sin\beta}{(d/\sin\beta) - L_c} \right] \quad (6)
 \end{aligned}$$

$$\begin{aligned}
 T_{e2} &= \frac{\epsilon V_4^2 W}{2\beta^2} \int_{L_c}^{L_c+L_{eff}} \frac{y}{((d/\sin\beta) + y)^2} dx \\
 &= \frac{\epsilon V_4^2 W}{2\beta^2} \left[ \ln \left| \frac{d}{\sin\beta} + L_\beta \right| + \frac{d/\sin\beta}{(d/\sin\beta) + L_\beta} \right. \\
 &\quad \left. - \ln \left| \frac{d}{\sin\beta} + L_c \right| - \frac{d/\sin\beta}{(d/\sin\beta) + L_c} \right] \quad (7)
 \end{aligned}$$

where  $d$  is the distance from the rotation axis of the mirror to the substrate,  $L_\beta$  the length from the rotation axis of the mirror to the effective length of the attraction plates:

$$L_\beta = L_c + L_{eff}$$

where  $W$  is the width of the attraction plate:

$$V_3 = V_{dco} + v_y$$

$$V_4 = V_{dco} - v_y$$

The mechanical torque is:

$$T_m = 2 \frac{Gwt^3}{3l} \beta \left[ 1 - \frac{192}{\pi^5} \frac{t}{w} \tanh\left(\frac{\pi w}{2t}\right) \right] \quad (8)$$

The maximum scanning angle for a specific driving voltage is determined from the equilibrium point between Eqs. (5) and (8). The width of the outer torsion bars is 6  $\mu\text{m}$ , the thickness is 1.1  $\mu\text{m}$ , and the length is 200  $\mu\text{m}$ .

When the scanner is in 2-D scanning operation, it is subject to additional electrostatic torques about the  $x$ -axis. It is expected that the electrostatic forces acting on mirror also contribute electrostatic torques to rotate the attraction plate about the  $x$ -axis. The overall electrostatic torques is a superposition of the 1-D outer attraction electrostatic torques with contribution from the inner electrodes of the mirror:

$$\begin{aligned}
 T_{outer} &= T_{e1} - T_{e2} - \frac{1}{2} \epsilon_0 V_i^2 \\
 &\quad \times \iint_S y \left( \frac{\sin\gamma}{\gamma} \frac{1}{d - y \cos\beta \sin\alpha + x \sin\beta} \right)^2 dS \quad (9)
 \end{aligned}$$

When the scanner was instructed to perform multiple 2-D perimeters scans, it is observed that the additional torques has negligible effects on the linearity of the  $\beta$ -scans. Fig. 6 shows the perimeter scans of the scanner when it is biased at various direct current (dc) voltages. The  $\alpha$ - and  $\beta$ -scans show good linearity. Fig. 7 illustrates that the  $\beta$  angle of the scanner, when the outer electrodes are biased at a specific voltages  $v_y$ , is maintained regardless of the  $\alpha$ -scan modulating driving voltages,  $v_x$ , of the inner electrodes.

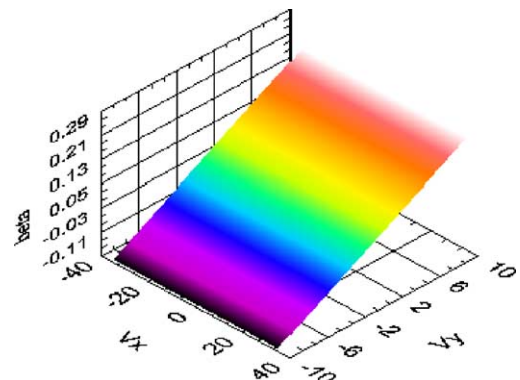


Fig. 7. Linearity of the  $\beta$ -scan is preserved even when the mirror is also subject to modulating  $v_x$  for  $\alpha$ -scan.

## 5. Device implementation

It has been demonstrated that surface micromachined polysilicon mirror exhibits significant curvature due to residual stress of the deposited thin films [19,20]. OCT is an interferometry technology; therefore, the flatness and topology of the large mirror deserve considerable attention so as to minimize any distortions of the light wavefronts. A hybrid bulk/surface micromachining process with dry etch release method to fabricate the high performance micro mirror has been developed. The single crystalline silicon serves as the mirror's mechanical reinforcement counteracting any residual stress of thin films deposited on it.

The fabrication process of the 2-D scanner is shown in Fig. 8. The SEM pictures of the scanner and close-up view of the torsion bars are shown in Fig. 9. (a) (100) Silicon substrate of 310  $\mu\text{m}$  thickness is deposited with 1 and 2  $\mu\text{m}$  of oxide by plasma enhanced chemical vapour deposition (PECVD) on the front and backsides of the Si substrate. The frontside oxide acts as both an electrical insulation and etch-stop layer for subsequent etching. The backside oxide acts as masking layer during the deep reactive ion etching (DRIE) of Si substrate. (b) On top of the frontside oxide, 1.1  $\mu\text{m}$  low stress silicon nitride is deposited by PECVD on the frontside as the torsion bar material. (c) Subsequently, 50  $\text{\AA}$  of titanium (Ti) and 2000  $\text{\AA}$  of aluminum (Al) are evaporated onto the silicon nitride to act as adhesive and reflective materials. (d) The Ti and Al metal layers are wet etched using Transene Type A aluminum etch solution to define the mirror and attraction plates. (d') This is the cross-sectional view of the device when rotated by 90°. The frontside silicon nitride and oxide are etched by reactive ion etching (RIE) to further define the mirror and attraction plates, and expose the underlying oxide etch-stop layer. From the initial 1  $\mu\text{m}$  of oxide deposited, a layer of 0.5  $\mu\text{m}$  oxide is intentionally left to act as an etch-stop layer. The thin layer of oxide also acts as a membrane that holds the scanner structure and torsion bars intact by minimizing mechanical shocks during human handling. (e) The backside oxide is patterned and etched through to expose the silicon substrate directly underneath the entire scanner structure. (f) The exposed silicon substrate is patterned with thick photoresist to protect the backside of the attraction plates and mirror area. (g) The attraction plates and mirror are defined by DRIE from the backside. The depth of the DRIE trenches around the mirror, and attraction plates is 32  $\mu\text{m}$ . (h) The backside photoresist is stripped away and the Si substrate is etched by DRIE until the frontside etch-stop oxide is exposed. It is noticed that DRIE has a slower etch rate in the narrow trenches around the scanner structure. Therefore, prolonged etching is required to fully expose the etch-stop oxide over the trench. As a result, a height of about 20  $\mu\text{m}$  Si material is left as mirror flatness enforcement. The release step is a major challenge because the mirror (1000  $\mu\text{m} \times 1000 \mu\text{m}$ ) is suspended by two inner torsion bars of dimensions, 1.1  $\mu\text{m} \times 6 \mu\text{m} \times 100 \mu\text{m}$ , and the entire scanner structure (1400  $\mu\text{m} \times 1700 \mu\text{m}$ ) is suspended in free-space by two outer torsion

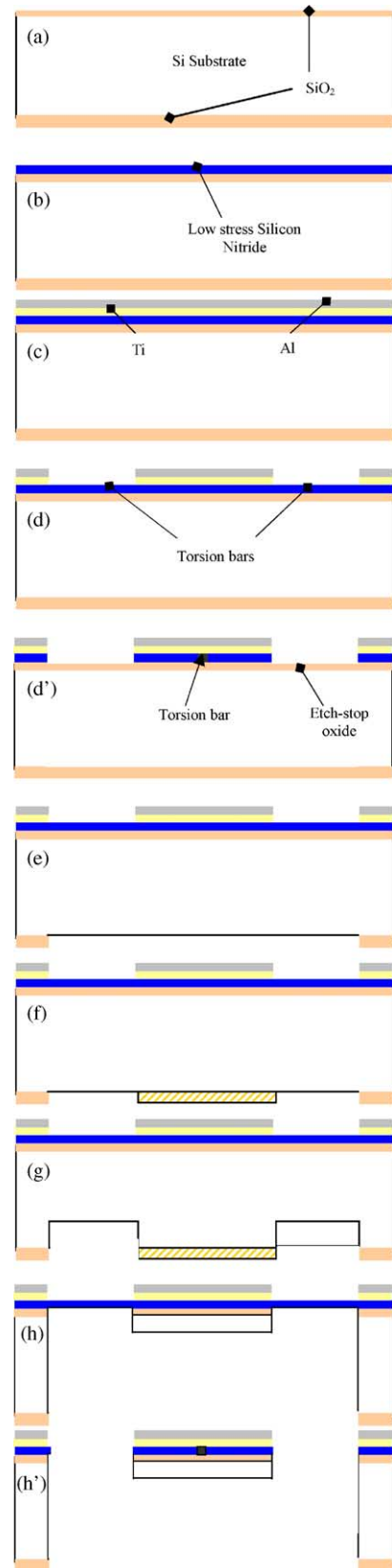


Fig. 8. Fabrication process of micro scanner.

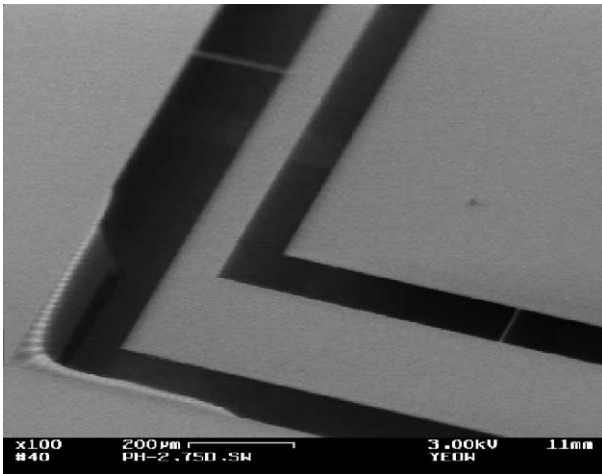


Fig. 9. SEM micrograph of the mirror and attraction plates suspended by two pairs of torsion bars. The inner torsion bars are  $100\ \mu\text{m} \times 6\ \mu\text{m} \times 1.1\ \mu\text{m}$ . The outer torsion bars are  $200\ \mu\text{m} \times 6\ \mu\text{m} \times 1.1\ \mu\text{m}$ .

bars of dimensions  $1.1\ \mu\text{m} \times 6\ \mu\text{m} \times 200\ \mu\text{m}$ . (h') This is the cross-sectional view of the device when rotated by  $90^\circ$ . Mirror is released by RIE etching of the thin etch-stop oxide layer from the frontside. A high-yield and reliable dry release technique is demonstrated.

### 6. Experiments

An experimental facility is set up to characterize the 2-D micromachined scanner. A 543.5 nm green HeNe laser, which provides the light source, is coupled into a single-mode fiber. A terminal GRIN lens is used to collimate the laser beam. A position sensitive detector (PSD OT-301) is used to determine the position of the reflected laser spot. The data from PSD is digitized by a National Instruments (NI-6711) analog I/O card and analyzed on a personal computer. The analog I/O card outputs user defined waveforms to act as driving voltages for the micromachined scanner. However, the maximum output voltages of  $\pm 10\ \text{V}$  from the I/O card are insufficient to generate the required electrostatic field strength. A total of four high voltage operational amplifiers are used to amplify the output voltages from the I/O card. The two pairs of complementary driving voltages ( $V_1, V_2$ , and  $V_3, V_4$ ) are connected to the inner and outer electrodes via the bonding pads of the scanner. The maximum amplified voltage is 100 V due to the limitation of the raiting voltages provided by the power supplies. The open loop control system used to characterize the micromachined scanner is shown in Fig. 10. The amplitude and frequency of the driving voltages are varied to change the  $\alpha$ - and  $\beta$ -scan patterns.

Fig. 11 illustrates the various scan patterns to demonstrate the flexibility of the micromachined scanner. The resonant frequency of the outer attraction plates is 181 Hz and that of the mirror is 45 Hz.

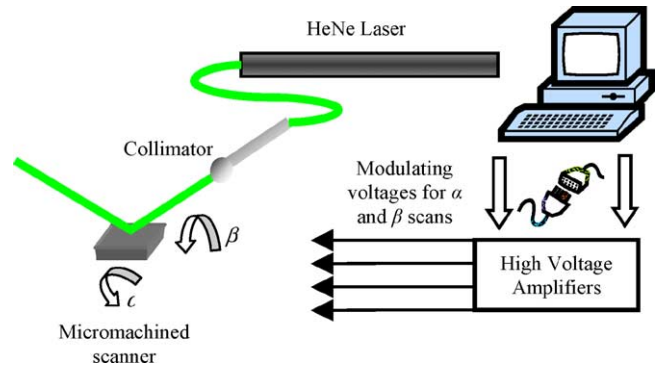


Fig. 10. Optical setup to characterize the micromachined scanner.

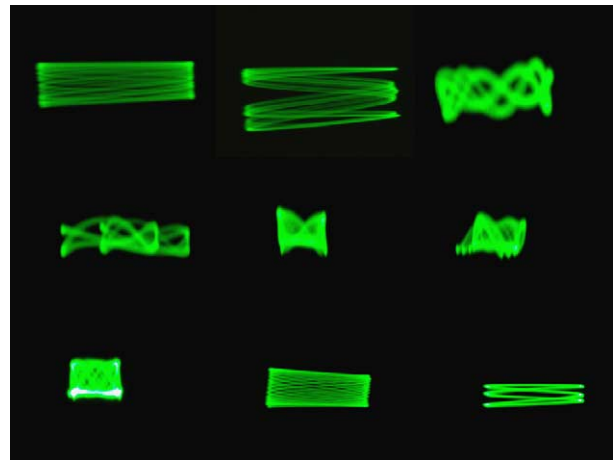


Fig. 11. Flexibility of the 2-D scanner is demonstrated by its scan patterns.

The 2-D scanner is integrated with an OCT system [23], as shown in Fig. 12. The system uses a broadband light source centred at 1300 nm with 63 nm (FWHM) bandwidth, providing a coherence length of  $\sim 13\ \mu\text{m}$  in air. The total output power is  $\sim 16\ \text{mW}$ . The reference arm of the OCT system provides the  $z$ -axis scanning at 8 kHz. The sample

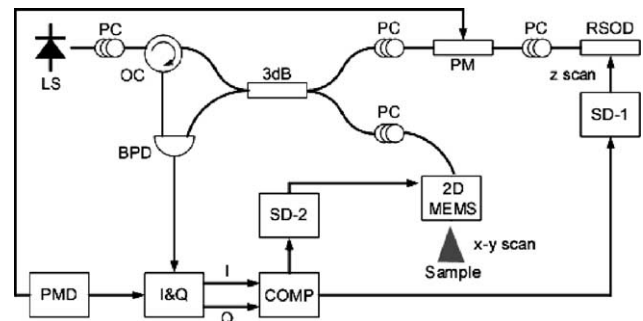


Fig. 12. Schematics of the 2-D micromachined scanner integrated with a high speed OCT system. LS: light source, PC: polarization controller, OC: optical circulator, BPD: balanced photo-detector, 3dB: fiber coupler, PM: phase modulator, RSOD: rapid scanning optical delay, PMD: phase modulator driver, I&Q: in-phase and quadrature demodulator, COMP: computer, SD-1,2: scan drivers for synchronizing the  $x$ -y and  $z$  scans.

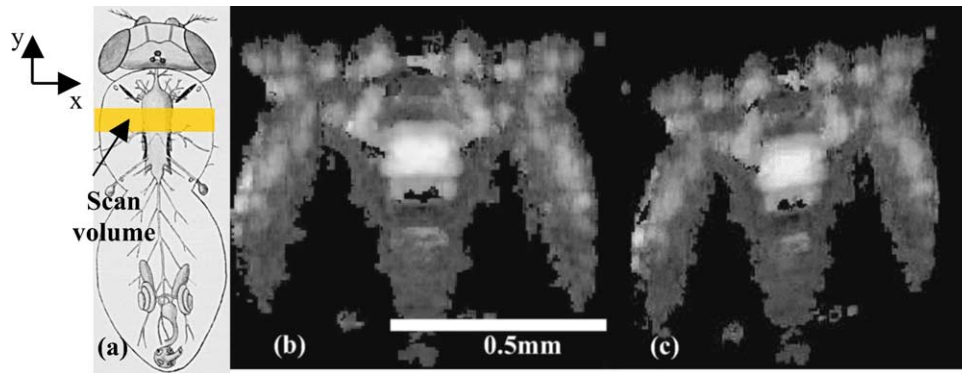


Fig. 13. (a) Anatomy of a *Drosophila melanogaster*; (b) OCT 3-D image of a fruit fly (*Drosophila melanogaster*) based on a 2-D micromachined scanner; (c) oblique view of the 3-D image.

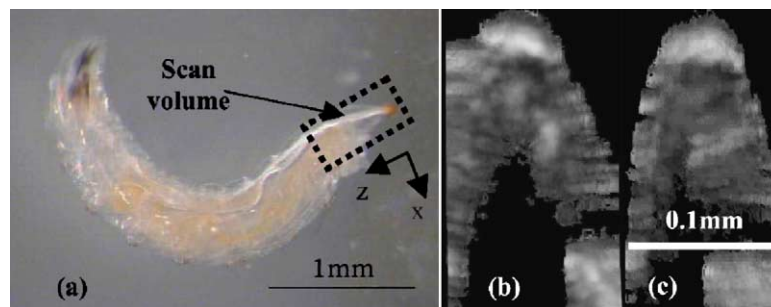


Fig. 14. (a) Image of a larva; (b) OCT 3-D image of a larva based on a 2-D micromachined scanner; (c) oblique view of the 3-D image.

arm consists of a 1 mm diameter GRIN lens positioned at  $45^\circ$  to the micromachined mirror, with a working distance of  $\sim 4$  mm and spot size of  $\sim 35 \mu\text{m}$ . The 3-D volume scans are achieved by a combination of axial ( $z$ ) scans at 8 kHz by the OCT system, the transverse ( $x$ ) scans at 56 Hz and longitudinal ( $y$ ) scans at 0.5 Hz by the micromachined 2-D scanner.

Experiments were conducted to characterize the micromachined-based OCT imaging performance. 3-D images were reconstructed from successive planar images (axial and transverse scans) during a single longitudinal scan of the micromachined scanner. An imaging volume of  $0.7 \text{ mm} \times 0.2 \text{ mm} \times 1 \text{ mm}$  with  $112 \times 143 \times 512$  pixels is acquired within 2 s. Fig. 13(a) shows the imaged volume of interest on a fruit fly (*Drosophila melanogaster*). The micromachined scanner provides the 2-D scan on the  $x$ - $y$  plane, simultaneously with the OCT system scans in the axial direction ( $z$ -axis). Fig. 13(b) shows a 3-D image of the internal organs of the sample. Wings structures of the fruit fly are clearly visible on the top left and right hand corner of the image. Fig. 13(c) illustrates the 3-D OCT image of the fruit fly from a different angle. Fig. 14(a) and (b) shows the microstructural features in the head of the larva and its internal organs. Fig. 14(c) shows the 3-D image from an oblique angle.

## 7. Conclusions

We have presented the mathematical models, fabrication process and integration of the 2-D micromachined scanner with the OCT imaging system. 3-D OCT images of fruit fly (*Drosophila melanogaster*) and its larva are demonstrated using the micromachined-based OCT system. There is ongoing research on the packaging and integration of the micro scanner device within an endoscope for clinical studies.

## Acknowledgment

The fabrication was carried out at the Cornell Nanofabrication Facility (CNF). The authors would like to acknowledge Richard Whitham, Princess Margaret Hospital for electronics support. This work was funded by the Natural Science and Engineering Research Council of Canada, the Canadian Institutes for Health Research, the Canadian Foundation for Innovation, and Photonics Research Ontario.

## References

- [1] N.C. McMillan, Developments in imaging. An historical review, *Scott Med. J.* 44 (1999) 180–185.

- [2] B.C. Wilson, Photodynamic therapy for cancer: principles, *Can. J. Gastroenterol.* 16 (2002) 393–396.
- [3] J.D. Fonger, Review: integrated myocardial revascularization, *Eur. J. Cardiothorac. Surg.* 16 (1999) 12–17.
- [4] S. Reiss, BioMEMS: a paradigm shift in the making, *Biophotonics* (2000) 40–45.
- [5] J.G. Fujimoto, C. Pitris, S.A. Boppart, M.E. Brezinski, Optical coherence tomography: an emerging technology for biomedical imaging and optical biopsy, *Nature* 2 (2000) 9–25.
- [6] V.X.D. Yang, I.A. Vitkin, L. WongKeeSong, B.C. Wilson, Endomicroscopy, Patent pending, June 2000.
- [7] A. Rollins, M. Kulkarni, S. Yazdanfar, In vivo video rate optical coherence tomography, *Opt. Express.* 3 (1998) 219–229.
- [8] H. Kiang, O. Solgaard, K.L. Lau, Electrostatic combdrive-actuated micromirrors for laser-beam scanning and positioning, *IEEE J. Microelectromech. Syst.* 7 (1998) 27–37.
- [9] A. Conant, P.M. Hagelin, U. Krishnamoorthy, M. Hart, O. Solgaard, K.Y. Lau, R.S. Muller, A raster-scanning full-motion video display using polysilicon micromachined mirrors, *Sens. Actuators* 83 (2000) 291–296.
- [10] Y.T. Pan, H.K. Xie, G.K. Fedder, Endoscopic optical coherence tomography based on a microelectromechanical mirror, *Opt. Lett.* 26 (2001) 1966–1968.
- [11] D.L. Dickensheets, G.S. Kino, Silicon-micromachined scanning confocal optical microscope, *IEEE J. Microelectromech. Syst.* 7 (1998) 38–47.
- [12] R.A. Conant, P.M. Hagelin, U. Krishnamoorthy, M. Hart, O. Solgaard, K.Y. Lau, R.S. Muller, A raster-scanning full-motion video display using polysilicon micromachined mirrors, *Sens. Actuators* 83 (2000) 291–296.
- [13] Y.T. Pan, H.K. Xie, G.K. Fedder, Endoscopic optical coherence tomography based on a microelectromechanical mirror, *Opt. Lett.* 26 (2001) 1966–1968.
- [14] V.A. Aksyuk, F. Pardo, C.A. Bolle, S. Arney, C.R. Giles, D.J. Bishop, Lucent microstar micromirror array technology for large optical crossconnects, *Proc. SPIE* 4178 (2000) 320–324.
- [15] H. Toshiyoshi, W. Piyawattanametha, C.-T. Chan, M.C. Wu, Linearization of electrostatically actuated surface micromachined 2-D optical scanner, *IEEE J. Microelectromech. Syst.* 10 (2001) 205–214.
- [16] U. Hofmann, S. Muehlmann, M. Witt, K. Dorschel, R. Schutz, B. Wagner, Electrostatically driven micromirrors for a miniaturized confocal laser scanning microscope, in: *SPIE Conference on Miniaturized Systems with Micro-Optics and MEMS*, Santa Clara, CA, USA, 20–22 September 1999.
- [17] S.P. Timoshenko, J.N. Goodier, *Theory of Elasticity*, third ed., McGraw-Hill, New York, 1970.
- [18] H. Toshiyoshi, H. Fujita, Electrostatic micro torsion mirrors for an optical switch matrix, *IEEE J. Microelectromech. Syst.* 5 (1996) 231–237.
- [19] J. Nee, R. Conant, K. Lau, T. Muller, Stretched-film micromirrors for improved flatness, in: *Proceedings of MEMS2000*, Miyazaki, Japan, 23–27 January, 2000.
- [20] D.L. Herington, J.J. Sniegowski, Improved polysilicon surface-micromachined micromirror devices using chemical-mechanical polishing, *Proc. SPIE* 3440 (1998) 148–153.
- [21] V.X.D. Yang, M.L. Gordon, S. Tang, N.E. Marcon, G. Gardiner, B. Qi, S. Bisland, E. Seng-Yue, S. Lo, J. Pekar, A. Mok, B.C. Wilson, I.A. Vitkin, High speed, wide velocity dynamic range Doppler optical coherence tomography. Part III. In vivo endoscopic imaging of blood flow in the rat and human gastrointestinal tracts, *Opt. Express.* 11 (2003) 2416–2424.
- [22] S. Tang, M.L. Gordon, V.X.D. Yang, M.E. Faughnan, M. Cirocco, B. Qi, E. Seng-Yue, G. Gardiner, G.B. Haber, G. Kandel, P. Kortan, I.A. Vitkin, B.C. Wilson, N.E. Marcon, In vivo Doppler optical coherence tomography of mucocutaneous telangiectases in hereditary hemorrhagic telangiectasia, *GI Endosc.* 58 (2003) 591–598.
- [23] V.X.D. Yang, M.L. Gordon, B. Qi, J. Pekar, S. Lo, E. Seng-Yue, A. Mok, B.C. Wilson, I.A. Vitkin, High speed, wide velocity dynamic range Doppler optical coherence tomography. Part I. System design, signal processing, and performance, *Opt. Express.* 11 (2003) 794–809.

## Biographies

*John T.W. Yeow* received his BAsC in electrical and computer engineering in 1997, MASc in 1999 and PhD in 2003 from mechanical and industrial engineering, all from the University of Toronto, Toronto, Canada. He is currently an assistant professor in the Department of Systems Design Engineering at the University of Waterloo, Waterloo, Canada. His research interests are in the development of micro and nanosystems for biomedical applications. He is a member of IEEE.

*Victor X.D. Yang* received his BAsC in biomedical engineering and MASc in electrical and computer engineering from University of Toronto in 1997 and 1998, respectively. He is currently pursuing a joint MD–PhD degree at the University of Toronto School of Medicine and Department of Medical Biophysics where his research concentrates on the development and applications of endoscopic Doppler optical coherence tomography. He is a member of the Canadian Medical Association and IEEE.

*Alain Chahwan* received his BAsC from mechanical and industrial engineering in 2003 at the University of Toronto. He is currently pursuing MASc in the Department of Mechanical Engineering at the University of California, Berkeley. His research interests are in MEMS.

*Maggie Gordon* is currently pursuing her MSc in the Department of Medical Biophysics at the University of Toronto, Toronto, Canada. Her research interests are in optical coherence/Doppler tomography for monitoring changes in normal and diseased tissues in response to radiation therapy.

*Bing Qi* received his BA in physics from Nanjing University in 1990, and PhD in optical instrument from Dalian University of Technology in 1996. From 1996 to 1999, he was a postdoc researcher in Department of Computer Science and Technology, Tsinghua University. During 1999–2002, he worked as a researcher scientist in the Center for Photonics Technology, Virginia Tech. From 2002 to 2003, he was a postdoc researcher in Ontario Cancer Institute/University Health Network. Currently, he is a postdoc researcher in Quantum Information Group, Department of Physics, University of Toronto. His current research concern is quantum cryptography.

*I. Alex Vitkin* received his BAsC from Queen University, Kingston, Canada, in 1985, his MASc in mechanical engineering from University of Toronto, Canada, in 1989, and his PhD in medical physics from McMaster University, Hamilton, Canada, in 1994. He is currently an associate professor in the Departments of Medical Biophysics and Radiation Oncology at the University of Toronto, a clinical physicist at the Princess Margaret Hospital, and an associate scientist at the Ontario Cancer Institute. His research interests are in biophotonics, and include photothermal effects in tissues, polarized light propagation in turbid media, and optical coherence tomography.

*Brian C. Wilson* is division head/professor of Medical Biophysics at the Ontario Cancer Institute/University of Toronto. He is also biomedical program director for Photonics Research Ontario and thrust leader for Health, Environment and Security for the Canadian Institute for Photonic Innovations. Since 1988, he has held the position of visiting professor at the Wellman Laboratories of Photomedicine, Harvard Medical School. He directs a broad basic-translational-clinical research program in biopho-

tonics that includes development of light-based techniques for clinical therapeutics, clinical diagnostics and micro-imaging.

*A.A. Goldenberg* received the BSc and MSc. degrees from Technion—Israel Institute of Technology, Haifa, Israel, in 1969 and 1972, respectively, and the PhD degree at the University of Toronto, Toronto, Ontario in 1976, all in electrical engineering. Since 1987, he has been a professor of mechanical engineering at the University of Toronto. He is a

past editor of the IEEE Transaction on Robotics and Automation, a fellow of the Institute of Electrical and Electronics Engineers, Inc. (IEEE), a fellow of the American Society of Mechanical Engineers (ASME), a member of the Professional Engineers of Ontario (PEO), and a designated consulting engineer of Ontario. His current research interests are in the field of MEMS, robotics and industrial automation, kinematics, control and dynamics of robots and dexterous end effectors.